Check for updates

View Article Online
View Journal

Journal of
Materials Chemistry B

Accepted Manuscript

This article can be cited before page numbers have been issued, to do this please use: N. Pachauri, K. Dave, A. K. Dinda and P. solanki, *J. Mater. Chem. B*, 2018, DOI: 10.1039/C8TB00653A.

This is an Accepted Manuscript, which has been through the Royal Society of Chemistry peer review process and has been accepted for publication.

Accepted Manuscripts are published online shortly after acceptance, before technical editing, formatting and proof reading. Using this free service, authors can make their results available to the community, in citable form, before we publish the edited article. We will replace this Accepted Manuscript with the edited and formatted Advance Article as soon as it is available.

You can find more information about Accepted Manuscripts in the author guidelines.

Please note that technical editing may introduce minor changes to the text and/or graphics, which may alter content. The journal's standard Terms & Conditions and the ethical guidelines, outlined in our author and reviewer resource centre, still apply. In no event shall the Royal Society of Chemistry be held responsible for any errors or omissions in this Accepted Manuscript or any consequences arising from the use of any information it contains.

ROYAL SOCIETY OF CHEMISTRY

rsc.li/materials-b

View Article Online
DOI: 10.1039/C8TB00653A

Cubic CeO_2 planted reduced graphene oxide based highly sensitive biosensor for non-invasive oral cancer biomarker

Namrata Pachauri[1ϕ],Kashyap Dave[1ϕ],Amit Dinda[2],Pratima R Solanki[1]*
[1]Special Centre for Nanoscience, Jawaharlal Nehru University, New Delhi-110067 India
[2]All India Institute of Medical Sciences, New Delhi-110608, India
E-mail: partima@mail.jnu.ac.in, pratimarsolanki@gmail.com; Tel: +91-11-26704740

Published on 06 April 2018. Downloaded by Freie Universitaet Berlin on 06/04/2018 16:55:19.

Journal of Materials Chemistry B Accepted Manuscript

ABSTRACT

Herein, results of cerium oxide nano cubes ($ncCeO_2$)-reduced graphene oxide (RGO) based nanocomposite were reported for detection of oral cancer biomarker, cytokeratin fragment-21-1(Cyfra-21-1) using the electrochemical technique. A nanocomposite of $ncCeO_2$-RGO was prepared by *in-situ* reduction of graphene oxide (GO) in the presence of $ncCeO_2$ using hydrazine hydrate. A Raman spectrum has confirmed the presence of $ncCeO_2$ in the matrix of RGO. The chemical composition of $ncCeO_2$-RGO nanocomposite was determined by X-ray photoelectron spectroscopy (XPS). X-ray diffraction (XRD) study has depicted the presence of crystalline $ncCeO_2$ and amorphous nature of RGO. Thin film of $ncCeO_2$-RGO composites was spin coated on the indium tin oxide (ITO) coated glass surface and used for co-immobilization of specific antibody Cyfra-21-1 by N-ethyl-N-(3-dimethyl aminopropyl) carbodiimide hydrochloride, N-hydroxysuccinimide (EDC-NHS) chemistry. Electrochemical response studies were monitored by using differential pulse voltammetry technique in the range of 0.625 pg mL^{-1} – 15 ng mL^{-1}. The best linear response was observed in the range of 0.625 pg mL^{-1} to 0.01 ng mL^{-1} with lower detection limit of 0.625 pg mL^{-1}. The sensitivity was found to be 14.5 µA ng^{-1} mL cm^{-2} with R^2 0.98 which was improved results as compared to the previously reported work. This BSA/Anti-Cyfra-21-1/$ncCeO_2$-RGO/ITO immunosensor shows selectivity towards Cyfra-21-1 in presence of glucose, sodium chloride, mucin 16, interleukin 8.

Keywords*:* Reduced graphene oxide; Cerium oxide Nanocubes; Cyfra-21-1, Oral cancer; immunosensor

View Article Online
DOI: 10.1039/C8TB00653A

Published on 06 April 2018. Downloaded by Freie Universitaet Berlin on 06/04/2018 16:55:19.

Journal of Materials Chemistry B Accepted Manuscript

ϕ: Both are equal contributors.

1. Introduction

Cerium oxide (CeO_2) nanomaterial, rare earth metal oxide, has considerable attention for the fabrication of point-of-care (POC) devices for global health and environment monitoring since last two decades. Due to their extraordinary properties such as, chemical inertness, nontoxic, large surface area, negligible swelling, electrical conductivity, wide band gap (3.4 eV), high isoelectric point (IEP 9.0), biocompatibility[1, 2, 3] high oxygen transfer ability and excellent catalytic property,[4, 5] grabbed the interest of researchers. However, due to high surface area, NPs have tendency to aggregate that reduces its properties. Thus dispersibility and conductivity is an issue that can be improved with supporting matrixes such as graphene and reduced graphene oxide (RGO) like materials. It has been found that the RGO as a suitable matrix for synthesis of nanocompsite with CeO_2 NPs.[6] CeO_2 NPs can be distributed/anchor onto basal plane of RGO, resulted in enhanced dispersion due to synergistic effect. Moreover, integration of CeO_2 NPs with RGO by a direct self-assemble approach, Van-der-Waals interactions occurred between the oxygen moiety present on CeO_2 NPs and basal plane or edges of RGO that provide 2-D structure with outstanding electron transfer capacity and large surface area. Moreover, availability of abundant functional groups on basal planes or on edges of RGO facilitates the binding of biomolecules for biosensor application for POC devices.

This CeO_2-RGO nanocomposite proved a promising electrochemical platform because it provide more exposed surface area and due to conducting nature of RGO resulted in fast electron transfer between the electrode and electrolyte and hence enhanced the catalytic efficiency.[7, 8] Moreover, enhancement of oxygen moieties in CeO_2-RGO composite due to control of restacking of RGO sheet, which increase the stability of nanocomposite.[6] Advantages of both (CeO_2 and RGO sheet) will be fully utilized in this composite as

View Article Online
DOI: 10.1039/C8TB00653A

Published on 06 April 2018. Downloaded by Freie Universitaet Berlin on 06/04/2018 16:55:19.

increased oxygen vacancy concentration of CeO_2 and conductivity of RGO *via* synergistic effect. A ncCeO_2-RGO composite was synthesized by hydrothermal route using *in-situ* nucleation of CeO_2 nanostructures in the presence of GO at 180°C.[9] Recently, Verma et al., modified the surface of GO by ceria using hydrothermal route at 220°C in the presence of CTAB.[10] In these methods higher temperature has been used which causes defects and instability in the GO structure[11] and do not reduce oxygen functionalities completely as compared to chemical reduction. In the present work, ncCeO_2-RGO composite was synthesized using the wet chemical method at a very low-temperature range (80-90°C) and comparatively it is very easy and fast method. CeO_2 embedded RGO matrix has been used for energy storage[12], photocatalysis[13], electro-catalysis[14], high affinity[15] and electrochemical studies.[16] Recently, Huang et al., reported the RGO–CeO_2 nano cubes composites show enhanced photocatalytic activity for the degradation of methyleneblue (MB) under UV-light irradiation as compared with pristine CeO_2 NCs.[17] A highly uniform CeO_2 hollow nanospheres decorated on RGO were reported for excellent photocatalytic activity for methylene orange degradation.[18] Wang et al., has reported the CeO_2 NPs incorporated in the matrix of RGO/C_3N_4 for catalytic degradation of Rhodamine B[19] and stated that RGO serve as a conductive network for generation of an electron-hole pair. Cheng et al. synthesized Fe_3O_4@SiO_2@mCeO_2 microspheres with a mesoporous CeO_2 shell and applied them to rapidly identify phosphopeptides by combining their affinity and catalysis properties.[5] Besides this, graphene oxide (GO)–Fe_3O_4 and RGO–Fe_3O_4 composites shows good water dispersibility, high affinity and rapid magnetic response. They have used these nanocomposites for the effective immobilization of proteins and the enrichment of peptides, respectively.[15] Zirconium oxide modified RGO composite was used for ochratoxin A detection and achieved higher sensitivity.[6] They have reported that interface between metal oxides and RGO offers a higher rate of charge transfer than the individual materials. The

Journal of Materials Chemistry B Accepted Manuscript

View Article Online
DOI: 10.1039/C8TB00653A

Published on 06 April 2018. Downloaded by Freie Universitaet Berlin on 06/04/2018 16:55:19.

surface of graphene was functionalized by zinc oxide NPs and used as electrochemical glucose sensor, simultaneously used for photocatalytic degradation of MB dye in ethanol within the region of UV.[20, 21] Srivastava et al., reported that the CeO_2-RGO nanocomposite enhanced remarkable electrocatalytic activity due to synergistic effects between the RGO and CeO_2 NPs created by uniform distribution of NPs on the plane of RGO.[8] Controlled structure synthesis of RGO and CeO_2 NPs enhanced the optical and catalytic properties.[7] Most of RGO–CeO_2 nanocomposites have been studied for the optical and catalytic properties. Thus, there is a wide scope to explore the electrochemical properties of CeO_2–RGO nanocomposite for biosensor application and biomarkers detection.

Oral cancer is the fifth most widespread form of cancer in this world and it infects the neck and head of a human.[22] The survival rate of the patient is 30-35 %, when it diagnosed in advanced stages and early detection can improve the survival rate. To identify the biomarker, several techniques were used as capillary electrophoresis-mass spectrometry[23], high-performance liquid chromatography[24], radio immune assays[25], enzyme-linked immunosorbent assay[26] and reverse transcription polymerase chain reaction.[27] However, these techniques are time-consuming and require expensive devices and maintenance. Since last few decades, electrochemical biosensors are found suitable devices for point-of-care diagnosis especially for very low detection range of analytes[28] with the high sensitivity, selectivity, cost-effectiveness, and rapid detection.[29, 30]Among the various oral cancer biomarkers, Cyfra-21-1 protein has significant importance due to its availability in high concentration in the saliva sample.[31, 32] The cut-off level of the cyfra-21-1 biomarker of cytokeratin 19 is 3.8 ng mL^{-1} which can increase upto17.46 ± 1.46 ng mL^{-1} in case of an oral cancer patient.[33] Researchers have reported different strategies for fabrication of electrochemical biosensors for early detection of Cyfra-21-1 to achieve higher specificity, selectivity, sensitivity and low detection limit. Kumar et al., had used hafnium nanostructure

Journal of Materials Chemistry B Accepted Manuscript

View Article Online
DOI: 10.1039/C8TB00653A

Published on 06 April 2018. Downloaded by Freie Universitaet Berlin on 06/04/2018 16:55:19.

for detection of CYFRA 21-1 and found the detection range of 2-18 ng mL^{-1}.[32] 3-Aminopropyl triethoxysilane (APTES) modified ZrO_2 NPs were reported for detection of Cyfra-21-1 and sensitivity obtained as 2.2 mA mL^{-1} ng^{-1}.[34] Further, they have reported APTES-ZrO_2 modified RGO substrate for Cyfra-21-1 detection and reported sensitivity of 0.756 μA mL $ng^{-1}$with limit of detection as 0.122 ng mL^{-1}.[35] In our previous report, L-cysteine capped lanthanum hydroxide was used for the detection of Cyfra-21-1 and found the linear range of 0.001–10.2 ng mL^{-1}, detection of limit 0.001 ng mL^{-1} with sensitivity of 12.04 μA mL ng^{-1} cm^2.[33] Here, it is expected that use of ncCeO$_2$-RGO nanocomposite will improve the sensitivity and low detection limits.

In the present work, a novel nanocomposite comprising of cerium nanocubes (ncCeO$_2$) and *in situ* reduction of GO during the synthesis of nanocomposite at low temperature was reported. It has been found that ncCeO$_2$ enhanced potential due to bound by six active planes than other shapes.[20] These ncCeO$_2$, RGO and ncCeO$_2$-RGO nanomaterials were characterized using various techniques like UV-Visible spectroscopy, Raman spectroscopy, Fourier transform infrared spectroscopy (FTIR), XPS, XRD and transmission electron microscopy (TEM). A thin film of ncCeO$_2$-RGO was prepared onto ITO surface using spin coater. This ncCeO$_2$-RGO/ITO electrode was modified by the specific antibody against Cyfra-21-1 (Anti-Cyfra-21-1) for electrochemical detection of oral cancer biomarker Cyfra-21-1. This immunoelectrode showed the improved sensing parameters as wide detection range from 0.625 pg mL^{-1} to 15 ng mL^{-1}, the lower limit of detection 0.625 pg mL^{-1} and sensitivity of 14.5 μA ng^{-1} mL cm^{-2} as compared to previously reported electrochemical immunosensor for Cyfra-21-1 detection (Table1). Results indicated that ncCeO$_2$-RGO nanocomposite consider as a promising matrix for electrochemical biosensors application. To the best of our knowledge, this is the first report on ncCeO$_2$-RGO nanocomposite for immunosensor for biomarker detection.

Journal of Materials Chemistry B Accepted Manuscript

View Article Online
DOI: 10.1039/C8TB00653A

Published on 06 April 2018. Downloaded by Freie Universitaet Berlin on 06/04/2018 16:55:19.

2. Experimental Section

2.1 Materials

Cerous nitrate hexahydrate ($CeN_3O_9.6H_2O$), sodium phosphate dibasic (Na_2HPO_4), sodium phosphate monobasic (NaH_2PO_4) and sodium hydroxide (NaOH) procured from SRL. Ammonia solution (NH_3, 30%) and hydrazine hydrate ($N_2H_4.H_2O$, 80%) were obtained from Thomas Baker. Indium tin oxide (ITO) coated glass substrate with 1.1 mm thickness was acquired from Blazers, UK. Graphite flakes, bovine serum albumin, N-ethyl-N-(3-dimethylaminopropyl) carbodiimide hydrochloride (EDC), N-hydroxysuccinimide (NHS) were procured from Sigma-Aldrich. Potassium ferricyanide, potassium ferrocyanide and hydrogen chloride were acquired from Fisher Scientific. Potassium permanganate and hydrogen peroxide were purchased from Merck. Monoclonal antibodies specific towards Cyfra-21-1 (Anti-Cyfra-21-1) and Cyfra-21-1(antigen) were purchased from Raybiotech Inc. and My BioSource USA, respectively.

2.2 Synthesis of $ncCeO_2$ and $ncCeO_2$-RGO nanocomposite

Cubical CeO_2 was synthesized using some modification in the previously reported co-precipitation method.[36] 2.17 g of $CeN_3O_9.6H_2O$ (0.1M) was dissolved in 50 mL (25 mL ethanol + 25 mL deionized water) and stirred (500 rpm) at 50°C. Further, 30 mL of 3M ammonia was added dropwise into the mixture in 1 h and reaction kept for next 4 h at 50 °C.

After that, the solution was kept at room temperature for the cooling down. Precipitate was washed with 0.1M HCl, ethanol (99.9%) and deionized water several times by centrifugation and dry into oven at 60ºC for 6 h.

GO was synthesized by the modified Hummers method.[37] To synthesis $ncCeO_2$-RGO composites, 170 mg of GO was sonicated (Temperature; 30±5, Power; 100 W, Frequency; 40 kHz) for 2 h in 100 mL of deionized water using bath sonicator (OSCAR Ultrasonicator).

Journal of Materials Chemistry B Accepted Manuscript

View Article Online
DOI: 10.1039/C8TB00653A

Published on 06 April 2018. Downloaded by Freie Universitaet Berlin on 06/04/2018 16:55:19.

After complete dispersion of GO, 70 mg of $ncCeO_2$ was added into previous GO solution and again kept for sonication for 1 h. Further, in this mixture, 400 mL distilled water was added and stirred for 30 minutes. Subsequently, 500 µL of hydrazine hydrate was added drop-by-drop, and the temperature was maintained between 80–90^{0}C. This reaction kept for 24 h on stirring for complete reduction of GO in the presence of CeO_2 cubes. After the completion of the reaction, mixture was centrifuged (rpm; 7000-8000) and washed by HCl (0.5M), ethanol (99.9%) and deionised water several times and kept at 50^{0}C inside the oven to dry.

2.3 Preparation of $ncCeO_2$-RGO thin film onto ITO

For deposition, firstly, ITO (15×5 mm^2) coated glass were cleaned sequentially by ethanol, acetone and distilled water in the bath sonicator for 10 minutes at each step. Thin film of 1 mg mL^{-1} solution of $ncCeO_2$-RGO on ITO was deposited using spin coater (Vb Ceramics Consultants) by following two steps of the process. In the first step, 30 µL of the prepared solution was poured onto the (3×5 mm^{-2}) area of ITO using spin of 150 rpm for 60 sec and in second step 500 rpm for 60 sec. these, thin film coated electrodes, were kept overnight for dry at room temperature for the further modification.

2.4 Fabrication of Anti-Cyfra-21-1/$ncCeO_2$-RGO/ITO

Spin-coated $ncCeO_2$-RGO/ITO electrodes were modified by Anti-Cyfra-21-1 using several steps sequentially. In the first step each thin film was washed with distilled water. To activate the functional groups of $ncCeO_2$-RGO, mixture of EDC (0.4M, 5µL) and NHS (0.1M, 5µL) was uniformly spread over the washed film of $ncCeO_2$-RGO/ITO electrode surface and kept for 40 minutes under the humid chamber at ambient temperature. After that film was washed with PBS solution. Subsequently, 10 µL of Anti-Cyfra-21-1 (50 µg mL^{-1}) was immobilized over the activated surface of $ncCeO_2$-RGO/ITO electrode and kept for 5 h under the humid chamber at room temperature (25ºC). Where, NH_2 groups of Anti-Cyfra-21-1 covalently bound with activated COO^- of RGO by forming an amide (CO-NH) bond.[38] After that, Anti-

Journal of Materials Chemistry B Accepted Manuscript

View Article Online
DOI: 10.1039/C8TB00653A

Published on 06 April 2018. Downloaded by Freie Universitaet Berlin on 06/04/2018 16:55:19.

Cyfra-21-1/ncCeO$_2$-RGO/ITO immunoelectrode was washed using PBS solution and removed. In the next step, non-specific activated sites were blocked using 10 µL of bovine serum albumin (BSA, 50 µg mL^{-1}).[39] BSA/Anti-Cyfra-21-1/ncCeO$_2$-RGO/ITO immunoelectrodes were stored at 4°C until further used. Fig. 1 shows the schematic representation of BSA/Anti-Cyfra-21-1/ncCeO$_2$-RGO/ITO immunoelectrode fabrication with different steps.

2.5 Characterization Techniques

Absorbance spectra for all synthesized materials were obtained using T90 + UV/Vis spectrometer of PG instruments PVT Ltd. X-ray crystallographic (XRD) study was carried out using Rigaku D/Max 2200 diffractometer of CuKα radiation of λ = 1.5418 Å. Raman spectra was recorded using 532 nm laser of Enspectr. High-resolution transmission electron microscopy (HR-TEM, JEOLJEM-2200 FS, Japan) was used for the identification of the morphology and diffraction pattern of all the nanomaterials at 200 kV. Fourier transform infrared spectroscopy (FTIR) spectra were measured using Varian 7000 FTIR. X-ray photoelectron spectroscopy (XPS) was done on Oxford Instrument, with AlKα radiation (1486.7 eV), as an excitation source for the elemental analysis of ncCeO$_2$-RGO nanocomposite. A thin film of ncCeO$_2$-RGO was deposited onto ITO coated glass substrate using spin coater (VB Ceramic Consultants) instrument. Electrochemical studies were performed by using Autolab (Auto86014) instrument in phosphate buffer saline (PBS) containing 5mM $[Fe(CN)_6]^{3-/4-}$ as an electrolyte solution using three electrode system, where Ag/AgCl and platinum were used as reference and counter electrode, respectively and BSA/Anti-Cyfra-21-1/ncCeO$_2$-RGO/ITO immunoelectrode as working electrode.

3. Results and discussion

3.1 Physicochemical Characterizations

Journal of Materials Chemistry B Accepted Manuscript

View Article Online
DOI: 10.1039/C8TB00653A

Published on 06 April 2018. Downloaded by Freie Universitaet Berlin on 06/04/2018 16:55:19.

UV-Vis spectroscopy is used to study the optical properties of nanoparticles and carbon based nanocomposites. Fig. 2(a) showing the absorbance spectrum of GO, $ncCeO_2$, $ncCeO_2$-RGO dispersed in water. GO shows the two peaks at 226 and 303 nm of π-π* and n- π* transition respectively.[40] Fig.2(b) showing the absorbance of $ncCeO_2$ dispersed at 310 nm peak previously reported.[41] After reduction of GO by hydrazine hydrate the peak red shifted showing the conversion to RGO.[40] The $ncCeO_2$-RGO shows two peaks at 237 and 317 nm confirms the presence of RGO and CeO_2 characteristics in the composite Fig.2(c).[42]

Raman spectroscopy is a useful technique to analysis carbonic material, metal oxide and carbon-metal oxide composites.[43-45] Graphitic materials show two peaks in Raman spectrum D (~1360 cm^{-1}) and G (~1590 cm^{-1}) band corresponding to defects characteristics and sp^2 structure respectively.[40, 44] Fig.3A shows the Raman spectra of GO, RGO, $ncCeO_2$ and $ncCeO_2$- RGO nanocomposites. GO shows D and G band at 1357 and 1603 cm^{-1} respectively Fig.3A(a). $ncCeO_2$ have a single Raman peak at 463 cm^{-1} corresponding F_{2g} mode in Fig.3A(b).[46] Fig. 3A(c) $ncCeO_2$-RGO showing three different peaks, at 462 cm^{-1} because of $ncCeO_2$ and at 1345 and 1603 cm^{-1} corresponding to the RGO.[46, 47] The D/G intensity of $ncCeO_2$-RGO nanocomposite was found higher (~1.01) than the GO (~0.85). Results suggest that decrease in average size of sp^2 domain after reduction of exfoliated GO. Raman spectra confirm the successfully synthesis of GO, $ncCeO_2$ and $ncCeO_2$-RGO nanocomposite.

Fig. 3(B) shows the XRD spectra of GO, $ncCeO_2$ and $ncCeO_2$-RGO nanocomposite. GO has a sharp peak at 10º which is corresponding to (002) plane with interlayer spacing of 0.88 nm which indicate the presence of oxygen moieties.[46] XRD spectra of $ncCeO_2$ in Fig. 3B(b) are correspond to (111), (200), (220), (311), (222), (400), (331) and (420) planes which were typically face-centered cubic (fcc) structure of CeO_2. It is confirmed from International Centre for Diffraction Data (JCPDS 34-0394).$ncCeO_2$-RGO nanocomposites also have same planes which confirms the presence of $ncCeO_2$ in the matrix of RGO [Fig. 3B(c)].[8] Recently

Journal of Materials Chemistry B Accepted Manuscript

View Article Online
DOI: 10.1039/C8TB00653A

Published on 06 April 2018. Downloaded by Freie Universitaet Berlin on 06/04/2018 16:55:19.

Verma et al. observed the boarder in width of (111) plane in CeO_2-RGO composite compare to pristine CeO_2.[46] But we did not observe any effect on spectra.

Fig. 4(A-D) shows TEM, and HR-TEM images of the $ncCeO_2$ and $ncCeO_2$-RGO nanocomposite to identify the shape and structural morphology. Image (A) clearly shows the cubic structure of CeO_2 with some compact dispersion at 20nm scale. The cubic shape structure of CeO_2 clearly visualized at 1nm scale (Image B) and HR-TEM image revealed the crystallinity of $ncCeO_2$ which is in good agreement with XRD data. An interplanar spacing (d-value) was obtained as 0.27 nm, corresponds to XRD plane (200) of$ncCeO_2$.[48] These results indicate that the $ncCeO_2$ maintained the crystallinity within the $ncCeO_2$-RGO nanocomposite.[48] The $ncCeO_2$ were decorated onto the surface of RGO sheets as marked by arrow and some were entrapped inside the RGO sheets demonstrated in Image (C). The image (D) revealed the edges of $ncCeO_2$ as well as RGO sheet as marked by an arrow, indicated the intermingling of $ncCeO_2$ onto RGO flask sheet which confirms the nanocomposite formation *via* synergistic effect.

FTIR was helped to confirm the stretching, vibrations and presence of the respective functional groups. Fig. 5 shows the FTIR spectrum of $ncCeO_2$-RGO/ITO, Anti-Cyfra-21-1/$ncCeO_2$-RGO/ITO and BSA/Anti-Cyfra-21-1/$ncCeO_2$-RGO/ITO immunoelectrodes. In case of $ncCeO_2$-RGO/ITO, two essential peaks appeared at 1642 and 1538 cm^{-1} corresponds to the graphene material, which confirms the presence of RGO in the nanocomposite.[9] After the immobilization of the Anti-Cyfra-21-1 (antibodies) over the $ncCeO_2$-RGO/ITO electrode, the peak intensified at 1642 cm^{-1} due to the NH_2 amide bonding which proves that the antibodies attached successfully over the surface. Finally, peak at 1538 cm^{-1} almost disappeared after applying BSA over the Anti-Cyfra-21-1/$ncCeO_2$-RGO/ITO immunoelectrode which authenticated that unbound sites were completely blocked. Most dominant peaks were found after the Anti-Cyfra-21-1 immobilization at 2920 cm^{-1} and 2853

Journal of Materials Chemistry B Accepted Manuscript

View Article Online
DOI: 10.1039/C8TB00653A

Published on 06 April 2018. Downloaded by Freie Universitaet Berlin on 06/04/2018 16:55:19.

cm^{-1} due to asymmetric and symmetric stretching vibrations of C-H bond in $–CH_2$ group.[49] But after the BSA immobilization intensity of the peaks were decreased which may be due to the extra layer formation over the Anti-Cyfra-21-1/ncCeO_2-RGO/ITO immunoelectrode. The peak at 3264 cm^{-1} assigned to OH-stretching, became broad hump after the Anti-Cyfra-21-1 and BSA immobilization onto ncCeO_2-RGO/ITO electrode, due to the availability of water molecules.[6] These results confirm the successfully modified ncCeO_2-RGO/ITO electrode surface with the Anti-Cyfra-21-1 and BSA.

Figure 6(A) shows the complete survey spectrum of ncCeO_2-RGO nanocomposite by XPS measurements (at range 1000-0 eV). Fig. 6(A) shows the existence of C (C 1s), O (O1s), Ce (Ce3d, Ce 4d) which confirm the chemical composition of ncCeO_2-RGO nanocomposite. Fig. 6(B) shows deconvoluted XPS spectrum of C 1s where we identified the peaks at 284.5 eV, 285.5eV, 286.6 eV, 288.1 eV and 289.2eV binding energy which are assigned to (C=C),(C-C)/(C-H), (C-OX), (C=O)/(O-C-O) and C(=O)-OX.[40, 50] The peak position at about~284.5 eV is to responsible to (C-C)[8] and others are due to the oxygen-containing carbonaceous bands in ncCeO_2-RGO nanocomposite.[47,51] The O 1s spectrum [Fig. 6(C)] was deconvoluted into two peaks at about 529.5 eV and 531.7 eV which were assigned to Ce-O and Ce-O and OH, respectively.[51] XPS spectra of Ce 3d were deconvoluted to evaluate the presence of oxygen vacancy in ncCeO2-RGO composite in Fig.6(D). Observed peaks at 901.3 907.5, 916.9eV because of $3d_{3/2}$ of Ce^{+4} cations and 882.6, 889.0 and 898.5 eV $3d_{5/2}$ of Ce^{+4} cations. Two more peaks of 903.6 and 884.6 eV shows $3d_{3/2}$ and of $3d_{5/2}$ of Ce^{+3} cations.[52] These transformation of oxidation states from 4+ to 3+ in Ce was due to the formation of oxygen vacancy and loss of lattice oxygen.[46, 53]

3.2 Electrochemical Studies

The electrochemical sensor changes the nature of the response on the different type of pH electrolytes.[33] Thus, it was necessary to find the effect of pH on BSA/Anti-Cyfra-21-

Journal of Materials Chemistry B Accepted Manuscript

View Article Online
DOI: 10.1039/C8TB00653A

Published on 06 April 2018. Downloaded by Freie Universitaet Berlin on 06/04/2018 16:55:19.

1/ncCeO$_2$-RGO/ITO immunoelectrode in PBS containing $[Fe(CN)_6]^{3-/4-}$ electrolyte solution. DPV technique in the range of -0.3 V to 0.4 V at 50 mV s^{-1} step potential was used to monitored pH effect at different pH values (7.0, 7.2, 7.4, 7.6, 7.8, 7.9 and 8.1) of the electrolyte. It was observed that the magnitude of current increased from 7.0 to 7.4 and then decreased from 7.4 to 8.1 (Supplementary data; Fig. S1). Thus, the maximum (~ 82 µA) magnitude of current was obtained at pH 7.4 from the [Fig. 7(A)]. This change in current response decreased because of excess of H^+ and OH^- destroyed the characteristics of methyl parathion.[54] Thus, PBS (pH 7.4) was used for all electrochemical studies.

To optimize the required concentration of antibodies for sensor application, different concentrations (15, 25, 50, 75 and 100 µg mL^{-1}) of Anti-Cyfra-21-1 was prepared, and DPV studied performed under the same conditions (Supplementary data; Fig. S2). The change in peak current increase from 15 to 50 µg mL^{-1} then started decreasing, the maximum current (83µA) response obtained at 50 µg mL^{-1} [Fig. 7(B)]. Thus, the optimized concentration 50 µg mL^{-1} was used for all the electrochemical studies.

Electron transfer kinetics of the ncCeO$_2$/ITO, ncCeO$_2$-RGO/ITO, Anti-Cyfra-21-1/ncCeO$_2$-RGO/ITO and BSA/Anti-Cyfra-21-1/ncCeO$_2$-RGO/ITO was done using CV technique [Fig. 7(C)]. The magnitude of anodic peak current was found highest of ncCeO$_2$-RGO nanocomposite (curve iii; 0.224 mA) as compared to ncCeO$_2$/ITO (curve ii; 0.198 mA) and bare ITO (curve i; 0.206 mA). The magnitude of current of ncCeO$_2$/ITO is lower due to poor conductance of ncCeO$_2$. However, the magnitude of current of ncCeO$_2$-RGO nanocomposite was enhanced due to electrical conductive nature of RGO.[55] These results suggest the that the synergistic effect occurred between the excellent conductivity of RGO and catalytical behaviour of ncCeO$_2$.[8] Kumar et al. also reported the reduction in DPV current after deposition of ZrO$_2$ NPs on the ITO substrate and the enhancement in the current obtained with RGO-ZrO$_2$ composite.[35] However, after the immobilization of Anti-Cyfra-21-1over the

Journal of Materials Chemistry B Accepted Manuscript

View Article Online
DOI: 10.1039/C8TB00653A

Published on 06 April 2018. Downloaded by Freie Universitaet Berlin on 06/04/2018 16:55:19.

ncCeO$_2$-RGO/ITO electrode, the magnitude of current increased as compared to ncCeO$_2$-RGO/ITO (curve iv; 0.267 mA). Due to the covalent binding between the NH_2 group of Anti-cyfra-21-1 and carboxylic group (-COOH) of RGO which formed the penetrating path to speed up the electron transfer between Anti-Cyfra-21-1 and electrode.[56,57] Moreover, electrostatic interaction occurred between the freely available sites of antibodies with redox species $[Fe(CN)_6]^{3-/4-}$, resulted in fast electron mobility towards the electrode surface.[56, 58] Subsequently, the available unbound active sites over the Anti-Cyfra-21-1/ncCeO$_2$-RGO/ITO electrode surface were blocked by applying the BSA. So the electron transportation was hampered resulting in a decrease in current value (curve v; 0.237 mA). All of these steps confirm the modification of ncCeO$_2$-RGO/ITO electrode with biomolecules.

Further, the electrochemical response of all electrodes (ncCeO$_2$/ITO, ncCeO$_2$-RGO/ITO, Anti-Cyfra-21-1/ncCeO$_2$-RGO/ITO and BSA/Anti-Cyfra-21-1/ncCeO$_2$-RGO/ITO) was monitored using EIS studies [Fig. 7(D)], between the frequency ranges of 0.1 - 10^5 Hz under similar experimental conditions. It was found that all electrodes followed the similar trends in a change in the resistance value as monitored in [Fig. 7(C)]. Here, different characteristics including charge transfer resistance (R_{ct}), electrolyte resistance (R_s) and double layer capacitance (C_{dl}) of all modified electrodes were obtained from Nyquist plot fitted by the circuit as mentioned in graph [Fig. 7(D)] and obtained values were mentioned in Table 2, where R_{ct} reveals the insulating nature of the electrodes which confirms the stepwise electrode modification. Further, the value of R_{ct} of ncCeO$_2$/ITO was obtained as 2.32 KΩ which was slightly higher than the bare ITO electrode (1.80 KΩ) due to the decrease in electrical conductivity of ncCeO$_2$, that slow down the diffusion of redox species ($[Fe(CN)_6]^{3-/4-}$) towards the electrode surface. Further, the value of R_{ct} of ncCeO$_2$-RGO/ITO electrode decreased (1.42 KΩ) as compared to ncCeO$_2$/ITO and bare ITO electrode, which reveals the higher electrical conductivity and fast ions diffusion towards the electrode surface due to the

Journal of Materials Chemistry B Accepted Manuscript

View Article Online
DOI: 10.1039/C8TB00653A

Published on 06 April 2018. Downloaded by Freie Universitaet Berlin on 06/04/2018 16:55:19.

conductive nature of the RGO. However, R_{ct} value of Anti-Cyfra-21-1/ncCeO$_2$-RGO/ITO immunoelectrode decreased (1.35 KΩ) which determined the spatial orientation of the Anti-Cyfra-21-1 over the ncCeO$_2$-RGO/ITO electrode surface which helps in increasing the charge transfer between freely available NH_2 functional groups of anti-Cyfra-21-1and redox species ($[Fe(CN)_6]^{3-/4-}$).[34] After the BSA immobilization over the Anti-Cyfra-21-1/ncCeO$_2$-RGO/ITO immunoelectrode, the R_{ct} value increased as 1.45 KΩ, due to insulating nature of BSA and macromolecular structure that decreased the charge transfer between redox species $[Fe(CN)_6]^{3-/4-}$ and electrode surface by hindering.

The heterogeneous electron transfer rate constant (K_e) and time constant (τ) was calculated, as mentioned in the Table 2. The value of K_e was determined using equation S1 (Supplementary data). The value of K_e was obtained as 1.18×10^{-7} for the bare ITO that decreased to 0.91×10^{-7} for the ncCeO$_2$-RGO/ITO electrode due to the low electron transfer rate between the interface of the electrolyte solution and electrode surface. Subsequently, K_e value increased to 1.49×10^{-7} due to higher electron transfer rate because of the RGO. Similarly, after the Anti-Cyfra-21-1 immobilization over the ncCeO$_2$-RGO/ITO, K_e value increased to 1.57×10^{-7} which reveals the fast electron flow rate between the redox species and the immunoelectrode surface. However, value of K_e decreased to 1.46×10^{-7}, due to the insulating nature of the BSA onto Anti-Cyfra-21-1/ncCeO$_2$-RGO/ITO immunoelectrode,

Further, the time constant (τ) for all electrodes (ncCeO$_2$/ITO, ncCeO$_2$-RGO/ITO, Anti-Cyfra-21-1/ncCeO$_2$-RGO/ITO and BSA/Anti-Cyfra-21-1/ncCeO$_2$-RGO/ITO) was calculated using equation S2 (Supplementary data). The value of τ was determined as 2.82×10^{-3} for the bare ITO, and it increased for ncCeO$_2$/ITO (3.64×10^{-3}), and then decreased to 2.54×10^{-3} for the ncCeO$_2$-RGO/ITO electrode due to the fluctuations in electron transfer rate between the electrode surface and the redox species of the electrolyte. After the Anti-Cyfra-21-1 immobilization increased (3.05×10^{-3}) due to the fast diffusion of electrons generated from

Journal of Materials Chemistry B Accepted Manuscript

View Article Online
DOI: 10.1039/C8TB00653A

Published on 06 April 2018. Downloaded by Freie Universitaet Berlin on 06/04/2018 16:55:19.

the redox species. However, the value of τ again increased (3.90×10^{-3}) due to the insulating behaviour of BSA.[33, 34]

The scan rate studies of $ncCeO_2$-RGO/ITO as well as on BSA/Anti-Cyfra-21-1/$ncCeO_2$-RGO/ITO were recorded by CV from 10 to 100 mV s^{-1} scan rate at the potential range -0.5 – 0.5 V, to check the behaviour of redox species between the electrolyte and electrode surface [Fig.8 (A&B)]. In both cases ($ncCeO_2$-RGO/ITO and BSA/Anti-Cyfra-21-1/$ncCeO_2$-RGO/ITO), a linear variation in the magnitude of anodic (I_{pa}) and cathodic (I_{pc}) peak current occurred by increasing scan rate. These electrochemical reactions indicate diffusion control process.[56, 59] Fig. 8(A) and (B)**,** insets show the linear curve fitting graph of ($ncCeO_2$-RGO/ITO) and BSA/Anti-Cyfra-21-1/$ncCeO_2$-RGO/ITO observed the anodic and cathodic peak current along with the square root of scan rate. The linear equations (S3-S6) are mentioned in Supplementary data.

Randles-Sevcik equation (S7) was used for the determination of diffusion coefficient for redox species w.r.t. $ncCeO_2$-RGO/ITO and BSA/Anti-Cyfra-21-1/$ncCeO_2$-RGO/ITO immunoelectrode at the interface between electrolyte and electrode surface.[56] The value of D was calculated for ($ncCeO_2$-RGO/ITO; 8.82×10^{-12} cm^2 s^{-1}] and for BSA/Anti-Cyfra-21-1/$ncCeO_2$-RGO/ITO immunoelectrode [9.93×10^{-12} cm^2 s^{-1}].

3.2.1 Electrochemical Response Studies

The electrochemical response of Cyfra-21-1 antigen over the BSA/Anti-Cyfra-21-1/$ncCeO_2$-RGO/ITO immunoelectrode was recorded using DPV with different analyte concentration varying from 0.625 pg mL^{-1} to 15 ng mL^{-1}. During the electrochemical response studies, BSA/Anti-Cyfra-21-1/$ncCeO_2$-RGO/ITO immunoelectrode was treated with different concentration of Cyfra-21-1 and kept for 10 minutes for incubation. The electrochemical response current decreased with increase in the concentration of Cyfra-21-1 due to the formation of immunocomplex [Fig. 9(A)]. The immunocomplex created an electron transfer

Journal of Materials Chemistry B Accepted Manuscript

View Article Online
DOI: 10.1039/C8TB00653A

Published on 06 April 2018. Downloaded by Freie Universitaet Berlin on 06/04/2018 16:55:19.

blocking layer that slowed down the electron communication. Moreover, immunoelectrode started to become insulating in nature hindering the access of redox probe towards the electrode surface.[60] The mechanism behind the improved sensing performance of immunosensor that the incorporation of $ncCeO_2$ into RGO matrix provides a larger exposed surface area for electrochemical reaction of Cyfra-21-1. RGO is responsible for the enhancement of electrical conductivity result in fast mobility of electrons generated by redox species $[Fe(CN)_6]^{3-/4-}$ at the interface of electrode/electrolyte [Fig.9(D)].

In the present work the synthesis of composite with RGO solved the issues of dispercivity, electrical conductivity enhancement and biomolecules attachment. Moreover, the similar energy of 4f and 5d with low potential energy barrier makes the cerium for the possibility of change the oxidation states. This change in oxidation states is closely linked with the oxygen vacancies concentrations that make the CeO_2 for potential applicability in electrochemical application as sensor.

Fig. 9(B) shows a calibration plot between the peak current and concentrations of Cyfra21-1, shows two linear ranges as 0.625 $pgmL^{-1}$ to 0.01 $ngmL^{-1}$ and 0.01 to 15 $ngmL^{-1}$ as marked in the plot. Initially, the magnitude of current decreases linearly with increase of Cyfra21-1 concentrations varies from 0.625 pg mL^{-1} to 0.01 ng mL^{-1}. Results indicate that the Cyfra21-1 molecules rapidly interact with adequate anti-Cyfra-21-1 onto electrode surface. Moreover, fast response or immediate interaction occurred between the Cyfra-21-1 and BSA/Anti-Cyfra-21-1/$ncCeO_2$-RGO/ITO immunoelectrode. However, best linear range obtained from 0.625 pg mL^{-1} to 0.01 ng mL^{-1}, as low detection limit of 0.625 pg mL^{-1} and sensitivity as 14.54 μA ng^{-1} mL cm^{-2} with linear regression constant of 0.98. However, the magnitude of current was decrease slightly with an increase of Cyfra-21-1 concentration above 0.01 ng mL^{-1}, due to limited availability of free anti-Cyfra-21-1sites onto electrode surface and linear range obtained as 0.01 to 15 ng mL^{-1} and sensitivity of 2.6 μA ng^{-1}mL cm^{-2}.[61]The limit of

Journal of Materials Chemistry B Accepted Manuscript

View Article Online
DOI: 10.1039/C8TB00653A

Published on 06 April 2018. Downloaded by Freie Universitaet Berlin on 06/04/2018 16:55:19.

detection (LOD) was calculated by using formula LOD= 3σ/m; where σ is standard deviation of intercept and m is slop value in calibration curve.

These results confirm that the ncCeO$_2$-RGO based immunoelectrode exhibited the improved biosensing properties with detection range from the 0.625 pg mL^{-1} to -15 ng mL^{-1} as compared to our previous reported paper (1 pg mL^{-1} to 10 ng mL^{-1})[33]. Besides this, sensitivity is higher (14.54 μA mL ng^{-1} cm^{-2}) than the others reported in literature such as BSA/anti-Cyfra-21-1/L-Cys-La(OH)$_3$/ITO (12.04 μA mL ng^{-1} cm^{-2})[33]; BSA/anti-CYFRA-21-1/APTES/ZrO$_2$/ITO (0.756 μA mL ng^{-1})[35]; BSA/anti-Cyfra-21-1/APTES/nHfO$_2$/ITO (9.28 μA mL ng^{-1} cm^2)[32]. However, the lower detection limit is quite lower 0.625 pg mL^{-1} as compared to others 0.001 ng mL^{-1} (BSA/anti-Cyfra-21-1/L-Cys-La(OH)$_3$/ITO)[33]; 0.122 ngmL^{-1} (BSA/anti-CYFRA-21-1/APTES/ZrO$_2$-RGO/ITO)[35]; 0.21 ng mL^{-1} (BSA/anti-Cyfra-21-1/APTES/nHfO$_2$/ITO)[32]; 0.08 ng mL^{-1} (BSA/anti-CYFRA-21-1/APTES/ZrO$_2$/ITO)[34].

These results confirmed that the BSA/Anti-Cyfra-21-1/ncCeO$_2$-RGO/ITO immunoelectrode is highly sensitive towards the lower detection range. It means, this immunosensor is most suitable for the early detection of cancer biomarkers.

To check the utility of this immunosensor for real samples application, the BSA/Anti-Cyfra-21-1/ncCeO$_2$-RGO/ITO immunoelectrode was tested with the commercially available Cyfra-21-1 (standard) and spiked samples of fresh saliva of normal human's [Fig. 9(C)]. Spiked samples were prepared by collecting fresh normal human saliva where total volume 10 μL (5 μL of saliva + 5 μL varying concentration of Cyfra-21-10) from 0.625 pg mL^{-1}to 15 ng mL^{-1}. DPV response was monitored in the potential step range of -0.3 – 0.4 V at 50 mV s^{-1}. It was observed that the current decreased with increasing the concentration of spiked samples, but at the 15 ng mL^{-1} concentration it was near to standard Cyfra-21-1 samples. Results exhibited the good correlation between the current value of standard Cyfra-21-1 and spiked samples, with the relative standard deviation (RSD %) from 0.18-2.10%, which is the acceptable limit.

Journal of Materials Chemistry B Accepted Manuscript

View Article Online
DOI: 10.1039/C8TB00653A

Published on 06 April 2018. Downloaded by Freie Universitaet Berlin on 06/04/2018 16:55:19.

These results concluded that this BSA/Anti-Cyfra-21-1/ncCeO$_2$-RGO/ITO immunoelectrode are highly specific for Cyfra-21-1. Table 3 shows the values of RSD obtained with different concentrations of both standard and spiked samples.

3.2.2 Control Study, Selectivity and Reproducibility

The control experiment was conducted to monitor the effect of Cyfra-21-1 antigen on the ncCeO$_2$-RGO/ITO electrode (without antibodies). DPV response was monitored using concentrations range from 0.625 pg mL^{-1} to 0.1 ng mL^{-1} at same experimental conditions. Further, the magnitude of maximum peak current was found constant as ~ 80 μA with all concentrations of Cyfra-21-1 [Fig. 10(A)]. The magnitude of current does not change with varying concentrations of Cyfra-21-1 that confirms the no any types of interaction with the Cyfra-21-1 resulting in a specificity of Cyfra-21-1 towards the Anti-Cyfra-21-1.

Further, the selectivity of BSA/Anti-Cyfra-21-1/ncCeO$_2$-RGO/ITO immunoelectrode with specific Cyfra-21-1 was determined by monitoring the change in response with different interferents present in saliva samples such as NaCl (20 mM), glucose (7 mg mL^{-1}), MUC-16 (2 pg mL^{-1}), IL-8 (5 pg mL^{-1}) and cyfra-21-1 (0.01 ng mL^{-1})using DPV [Supplementary data; S3]. There were not much changes obtained with all interferents. However, small change in current value with cyfra-21-1 compared with other interferents depicted that the immunoelectrode is selectively fabricated for the cyfra-21-1 antigen [Fig. 10(B)].

Reproducibility of the BSA/Anti-Cyfra-21-1/ncCeO$_2$-RGO/ITO immunoelectrodes were monitored with a change in magnitude of current value using DPV with potential range -0.3-0.4 V at 50 mV s^{-1} step potential. Fig. 10 (C) shows the DPV curve of five electrodes and found a stable response with the 1.14% RSD which depicts the highest reproducibility of immunoelectrode.

The shelf-life of BSA/Anti-Cyfra-21-1/ncCeO$_2$-RGO/ITO immunoelectrode was monitored by DPV at the potential range -0.3 - 0.4 V. These electrodes were stored at 4^{o}C till 5 weeks

Journal of Materials Chemistry B Accepted Manuscript

View Article Online
DOI: 10.1039/C8TB00653A

Published on 06 April 2018. Downloaded by Freie Universitaet Berlin on 06/04/2018 16:55:19.

[Supplementary data; S4]. There was no change in current till 3 weeks after that negligible change was found till another two weeks. Thus, 82.14% stability response of the immunoelectrode was found till 5 weeks [Fig. 10(D)].

4. Conclusions

Here, a label-free, highly selective, very specific, sensitive and non-invasive immunoelectrode was reported for the early detection of oral cancer biomarker Cyfra-21-1 using ncCeO_2-RGO nanocomposite.TEM images confirm the cubic shaped CeO_2 nanomaterial's planted onto RGO substrate and maintained the crystallinity. Elemental analysis of ncCeO_2-RGO nanocomposite also confirms the successful formation of nanocomposite as analysed by XPS data. This nanocomposite proves an ideal material for electrochemical sensing platform because RGO provides the fast transfer of electron due to higher conductivity of RGO and ncCeO_2 provide a high surface to volume ratio for further surface modification by Anti-Cyfra-21-1 and enhanced catalytic properties. This immunosensor exhibits the specific detection of Cyfra-21-1 from 0.625pg mL^{-1} to 15 ng mL^{-1}, lowest detection limit 0.625 pg mL^{-1} with the increased sensitivity 14.54 μA ng^{-1} mL cm^{-2}. Moreover, this immunosensor can check the Cyfra-21-1 in saliva samples as observed by the good response with the spiked sample. The immunoelectrode does not exhibit any interferent's effect and found reproducible. The biosensing properties were found improved as compared to the previously reported in the literature.

Acknowledgement

This study was supported by a grant from the Department of Science and Technology [Nanomission Project; No. SR/NM/NS-1144/2013 (G)], Government of India. And we are thankful to AIRF, JNU which provided all characterization and also to Materials Research Centre, MNIT Jaipur for XPS characterization.

References

Journal of Materials Chemistry B Accepted Manuscript

View Article Online
DOI: 10.1039/C8TB00653A

Published on 06 April 2018. Downloaded by Freie Universitaet Berlin on 06/04/2018 16:55:19.

1. A. A. Ansari, P. R. Solanki and B. D. Malhotra, *Applied Physics Letters*, 2008, **92**, 263901.
2. C. Strobel, M. Forster and I. Hilger, *Beilstein J Nanotechnol*, 2014, **5**, 1795-1807.
3. S. Khan and A. A. Ansari, *Sci Technol Adv Mater*, 2017, **18**, 364-373.
4. S. Saha, S. K. Arya, S. P. Singh, K. Sreenivas, B. D. Malhotra and V. Gupta, *Biosensors and Bioelectronics*, 2009, **24**, 2040-2045.
5. G. Cheng, J. L. Zhang, Y.-L. Liu, D. H. Sun and J. Z. Ni, *Chemical Communications*, 2011, **47**, 5732-5734.
6. P. K. Gupta, S. Tiwari, Z. H. Khan and P. R. Solanki, *Journal of Materials Chemistry B*, 2017, **5**, 2019-2033.
7. L. Jiang, M. Yao, B. Liu, Q. Li, R. Liu, H. Lv, S. Lu, C. Gong, B. Zou, T. Cui, B. Liu, G. Hu and T. Wågberg, *The Journal of Physical Chemistry C*, 2012, **116**, 11741-11745.
8. M. Srivastava, A. K. Das, P. Khanra, M. E. Uddin, N. H. Kim and J. H. Lee, *Journal of Materials Chemistry A*, 2013, **1**, 9792-9801.
9. M. Srivastava, A. Kumar Das, P. Khanra, M. Elias Uddin, N. H. Kim and J. Lee, *Journal of Materials Chemistry A*, 2013, **1**, 9792-9801.
10. R. Verma and S. K. Samdarshi, *The Journal of Physical Chemistry C*, 2016, **120**, 22281-22290.
11. S. Eigler, M. Enzelberger-Heim, S. Grimm, P. Hofmann, W. Kroener, A. Geworski, C. Dotzer, M. Rockert, J. Xiao, C. Papp, O. Lytken, H. P. Steinruck, P. Muller and A. Hirsch, *Adv Mater*, 2013, **25**, 3583-3587.
12. X. Yang, C. Cheng, Y. Wang, L. Qiu and D. Li, *Science*, 2013, **341**, 534-537.
13. Y. Liang, H. Wang, H. Sanchez Casalongue, Z. Chen and H. Dai, *Nano Research*, 2010, **3**, 701-705.

Journal of Materials Chemistry B Accepted Manuscript

View Article Online
DOI: 10.1039/C8TB00653A

Published on 06 April 2018. Downloaded by Freie Universitaet Berlin on 06/04/2018 16:55:19.

14. Z. S. Wu, S. Yang, Y. Sun, K. Parvez, X. Feng and K. Müllen, *Journal of the American Chemical Society*, 2012, **134**, 9082-9085.

15. G. Cheng, Y. L. Liu, Z. G. Wang, J. L. Zhang, D. H. Sun and J.Z. Ni, *Journal of Materials Chemistry*, 2012, **22**, 21998-22004.

16. J. Li, D. Kuang, Y. Feng, F. Zhang, Z. Xu and M. Liu, *Journal of hazardous materials*, 2012, **201-202**, 250-259.

17. K. Huang, Y. H. Li, S. Lin, C. Liang, X. Xu, Y. F. Zhou, D. Y. Fan, H. J. Yang, P. L. Lang, R. Zhang, Y. G. Wang and M. Lei, *Materials Letters*, 2014, **124**, 223-226.

18. Y. Xu, Y. Zhang, Y. Zhou, S. Xiang, Q. Wang, C. Zhang and X. Sheng, *RSC Advances*, 2015, **5**, 58237-58245.

19. L. Wang, J. Ding, Y. Chai, Q. Liu, J. Ren, X. Liu and W.-L. Dai, *Dalton Transactions*, 2015, **44**, 11223-11234.

20. P. Norouzi, H. Ganjali, B. Larijani, M. Reza Ganjali, F. Faridbod and H. Ali Zamani, *Int. J. Electrochem. Sci.*, 6 (2011) 5189 - 5199, 2011.

21. T. Kavitha, A. I. Gopalan, K. P. Lee and S. Y. Park, *Carbon*, 2012, **50**, 2994-3000.

22. W. Tan, L. Sabet, Y. Li, T. Yu, P. R. Klokkevold, D. T. Wong and C. M. Ho, *Biosensors & bioelectronics*, 2008, **24**, 266-271.

23. W. Kolch, C. Neusüß, M. Pelzing and H. Mischak, *Mass Spectrometry Reviews*, 2005, **24**, 959-977.

24. R. Mateos, E. Lecumberri, S. Ramos, L. Goya and L. Bravo, *Journal of Chromatography B*, 2005, **827**, 76-82.

25. P. Collier, C. J. Watson, V. Voon, D. Phelan, A. Jan, G. Mak, R. Martos, J. A. Baugh, M. T. Ledwidge and K. M. McDonald, *European Journal of Heart Failure*, 2011, **13**, 1087-1095.

Journal of Materials Chemistry B Accepted Manuscript

View Article Online
DOI: 10.1039/C8TB00653A

Published on 06 April 2018. Downloaded by Freie Universitaet Berlin on 06/04/2018 16:55:19.

26. I. Dalle-Donne, R. Rossi, D. Giustarini, A. Milzani and R. Colombo, *Clinica Chimica Acta*, 2003, **329**, 23-38.

27. X. Chen, Y. Ba, L. Ma, X. Cai, Y. Yin, K. Wang, J. Guo, Y. Zhang, J. Chen, X. Guo, Q. Li, X. Li, W. Wang, Y. Zhang, J. Wang, X. Jiang, Y. Xiang, C. Xu, P. Zheng, J. Zhang, R. Li, H. Zhang, X. Shang, T. Gong, G. Ning, J. Wang, K. Zen, J. Zhang and C.-Y. Zhang, *Cell Res*, 2008, **18**, 997-1006.

28. M. Labib, E. H. Sargent and S. O. Kelley, *Chem Rev*, 2016, **116**, 9001-9090.

29. X. Kang, J. Wang, H. Wu, J. Liu, I. A. Aksay and Y. Lin, *Talanta*, 2010, **81**, 754-759.

30. D. Grieshaber, R. MacKenzie, J. Vörös and E. Reimhult, *Sensors*, 2008, **8**, 1400.

31. N. Jeiroodi, S. M.-J. Aslani, B. Khademi, M. Malekzadeh and Z. Jaafari- Ashkavandi, *Iranian Journal of Otorhinolaryngology*, 2017, **29**, 203-208.

32. S. Kumar, S. Kumar, S. Tiwari, S. Augustine, S. Srivastava, B. K. Yadav and B. D. Malhotra, *Sensors and Actuators B: Chemical*, 2016, **235**, 1-10.

33. S. Tiwari, P. Gupta, Y. Bagbi, T. Sarkar and P. Solanki, *Biosens Bioelectron.* 2017 15;891042-1052.

34. S. Kumar, S. Kumar, S. Tiwari, S. Srivastava, M. Srivastava, B. K. Yadav, S. Kumar, T. T. Tran, A. K. Dewan, A. Mulchandani, J. G. Sharma, S. Maji and B. D. Malhotra, *Advanced Science*, 2015, **2**, n/a-n/a.

35. S. Kumar, *Biosensors & bioelectronics*, 2016, **78**, pp. 497-504-2016 v.2078.

36. H. I. Chen and H. Y. Chang, *Ceramic International,* 2005,31 (6), 795-802.

37. J. Chen, B. Yao, C. Li and G. Shi, *Carbon*, 2013, **64**, 225-229.

38. J. Conde, J. T. Dias, V. Grazu, M. Moros, P. V. Baptista and J. M. de la Fuente, *Frontiers in chemistry*, 2014, **2**, 48.

Journal of Materials Chemistry B Accepted Manuscript

View Article Online
DOI: 10.1039/C8TB00653A

Published on 06 April 2018. Downloaded by Freie Universitaet Berlin on 06/04/2018 16:55:19.

39. S. Srivastava, M. A. Ali, S. Umrao, U. K. Parashar, A. Srivastava, G. Sumana, B. D. Malhotra, S. S. Pandey and S. Hayase, *Applied Biochemistry and Biotechnology*, 2014, **174**, 960-970.

40. K. Dave, K. H. Park and M. Dhayal, *RSC Advances*, 2015, **5**, 95657-95665.

41. X. Jiao, H. Song, H. Zhao, W. Bai, L. Zhang and Y. Lv, *Analytical Methods*, 2012, **4**, 3261-3267.

42. S. Kumar and A. Kumar, *Materials Science and Engineering: B*, 2017, **223**, 98-108.

43. A. C. Ferrari and J. Robertson, *Physical Review B*, 2000, **61**, 14095-14107.

44. A. C. Ferrari, J. C. Meyer, V. Scardaci, C. Casiraghi, M. Lazzeri, F. Mauri, S. Piscanec, D. Jiang, K. S. Novoselov, S. Roth and A. K. Geim, *Physical Review Letters*, 2006, **97**, 187401.

45. I. Kosacki, T. Suzuki, H. U. Anderson and P. Colomban, *Solid State Ionics*, 2002, **149**, 99-105.

46. L. Guo, Q. Zhong, J. Ding, Z. Lv, W. Zhao and Z. Deng, *RSC Advances*, 2016, **6**, 87869-87877.

47. S. Kumar, A. K. Ojha, D. Patrice, B. S. Yadav and A. Materny, *Physical Chemistry Chemical Physics*, 2016, **18**, 11157-11167.

48. L. Jiang, M. G Yao, B. Liu, Q. Li, R. Liu, H. Lu, S. Lu, C. Gong, B. Zou, T. Cui, G. Hu and T. Wågberg, *J. Phys. Chem. C*, **2012**, *116* (21), 11741–11745.

49. C. S. T. Araújo, E. I. Melo, V. N. Alves and N. M. M. Coelho, *Journal of the Brazilian Chemical Society*, 2010, **21**, 1727-1732.

50. W. MingYan, Z. Wei, Z. DongEn, L. ShuAn, M. WeiXing, T. ZhiWei and C. Jun, *Materials Letters*, 2014, **137**, 229-232.

51. R. Rajendran, L. K. Shrestha, K. Minami, M. Subramanian, R. Jayavel and K. Ariga, *Journal of Materials Chemistry A*, 2014, **2**, 18480-18487.

Journal of Materials Chemistry B Accepted Manuscript

View Article Online
DOI: 10.1039/C8TB00653A

52. Y. Yu, L. Zhong, Q. Zhong and W. Cai, *RSC Advances*, 2016, **6**, 50680-50687.

53. D. Joung, V. Singh, S. Park, A. Schulte, S. Seal and S. I. Khondaker, *The Journal of Physical Chemistry C*, 2011, **115**, 24494-24500.

54. G. Liu and Y. Lin, *Anal Chem*, 2005, **77**, 5894-5901.

55. C. Gómez-Navarro, R. T. Weitz, A. M. Bittner, M. Scolari, A. Mews, M. Burghard and K. Kern, *Nano Letters*, 2007, **7**, 3499-3503.

56. P. K. Gupta, N. Pachauri, Z. H. Khan and P. R. Solanki, *Journal of Electroanalytical Chemistry*, 2017, **807**, 59-69.

57. J. Conde, J. T. Dias, V. Grazú, M. Moros, P. V. Baptista and J. M. de la Fuente, *Frontiers in chemistry*, 2014, **2**, 48.

58. A. Vasudev, A. Kaushik and S. Bhansali, *Biosensors & Bioelectronics*, 2013, **39**, 300-305.

59. A. Kaushik, P. Solanki, M. Pandey, S. Ahmad and B. Malhotra, *Appl. Phys. Lett.*, 2009, **95**, 173703..

60. H. P. Peng, Y. Hu, A. L. Liu, W. Chen, X. H. Lin and X. B. Yu, *Journal of Electroanalytical Chemistry*, 2014, **712**, 89-95.

61. M. Masikini, N. S. Mailu, A. Tsegaye, N. Njomo, M. K. Molapo, O. C. Ikpo, E. C. Sunday, C. Rassie, L. Wilson, G. P. Baker and I. E. Iwuoha, *Sensors*, 2015, **15**.

Published on 06 April 2018. Downloaded by Freie Universitaet Berlin on 06/04/2018 16:55:19.

Journal of Materials Chemistry B Accepted Manuscript

View Article Online
DOI: 10.1039/C8TB00653A

Published on 06 April 2018. Downloaded by Freie Universitaet Berlin on 06/04/2018 16:55:19.

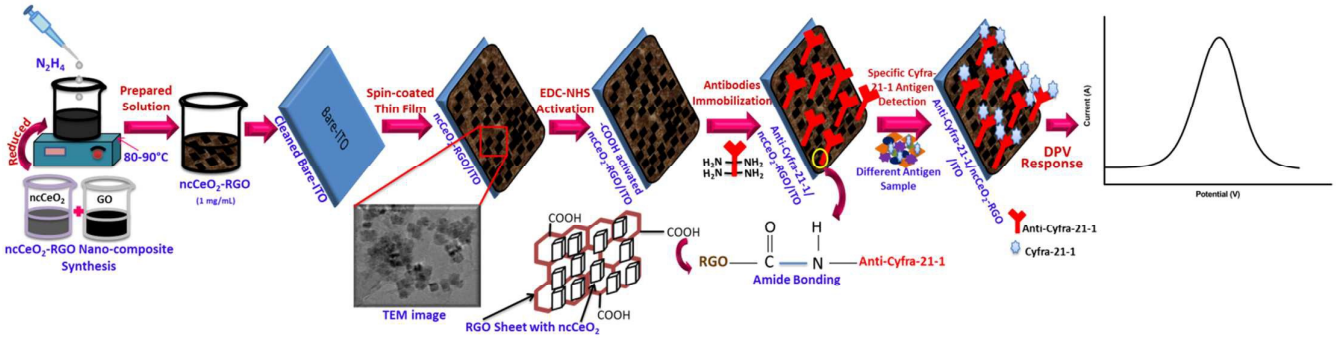

Figures

Fig. 1: Schematic represents the fabrication of BSA/Anti-Cyfra-21-1/$ncCeO_2$-RGO/ITO immunosensor with an electrochemical response.

Journal of Materials Chemistry B Accepted Manuscript

View Article Online
DOI: 10.1039/C8TB00653A

Published on 06 April 2018. Downloaded by Freie Universitaet Berlin on 06/04/2018 16:55:19.

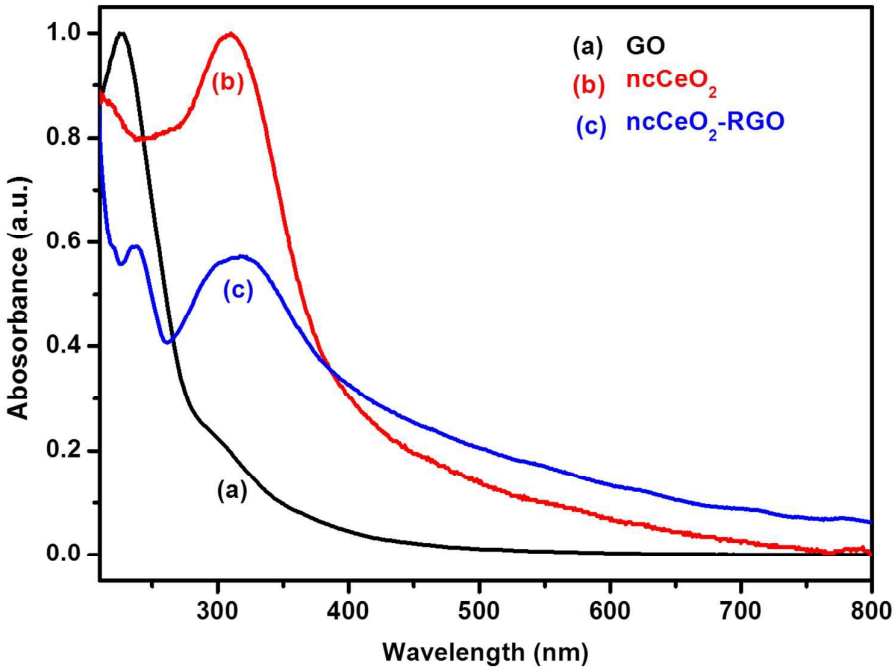

Fig. 2: UV-vis spectrum of (a) GO, (b) $ncCeO_2$ and (c) $ncCeO_2$-RGO.

Journal of Materials Chemistry B Accepted Manuscript

View Article Online
DOI: 10.1039/C8TB00653A

Published on 06 April 2018. Downloaded by Freie Universitaet Berlin on 06/04/2018 16:55:19.

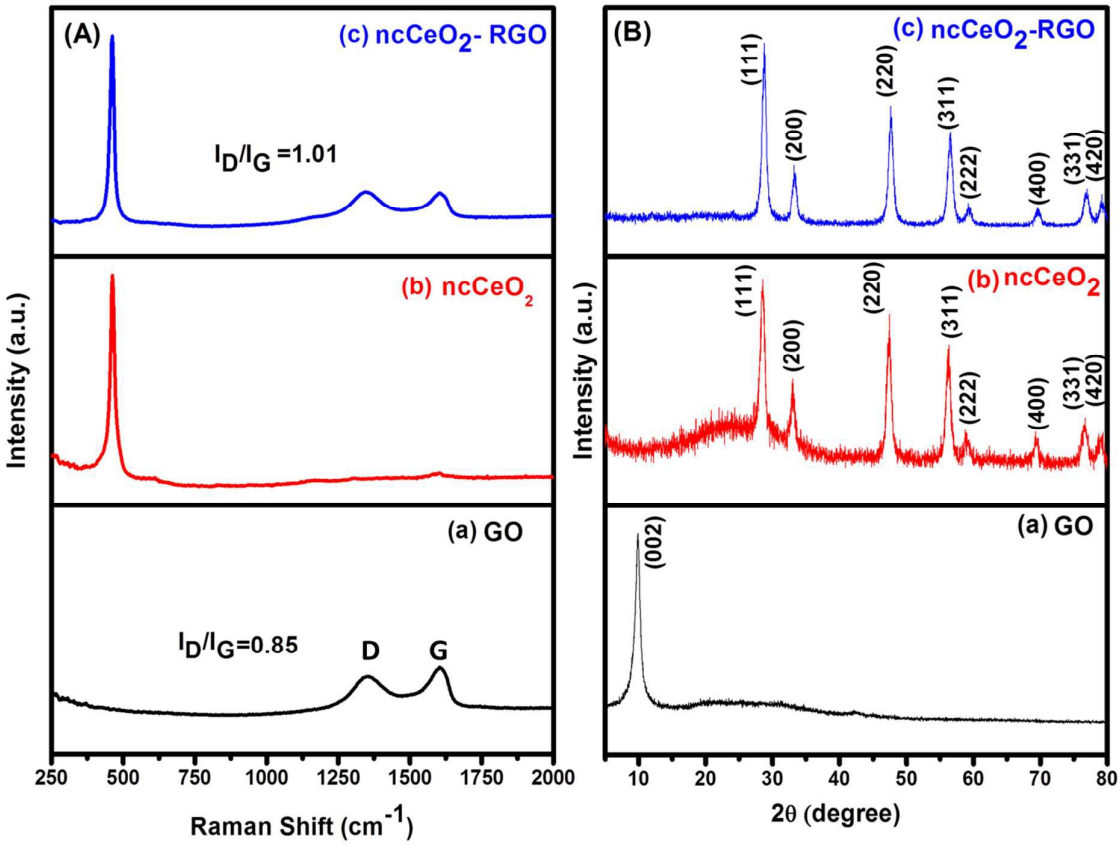

Fig. 3: (A) Raman shifts and (B) XRD pattern; GO, $ncCeO_2$ and $ncCeO_2$-RGO.

Journal of Materials Chemistry B Accepted Manuscript

View Article Online
DOI: 10.1039/C8TB00653A

Published on 06 April 2018. Downloaded by Freie Universitaet Berlin on 06/04/2018 16:55:19.

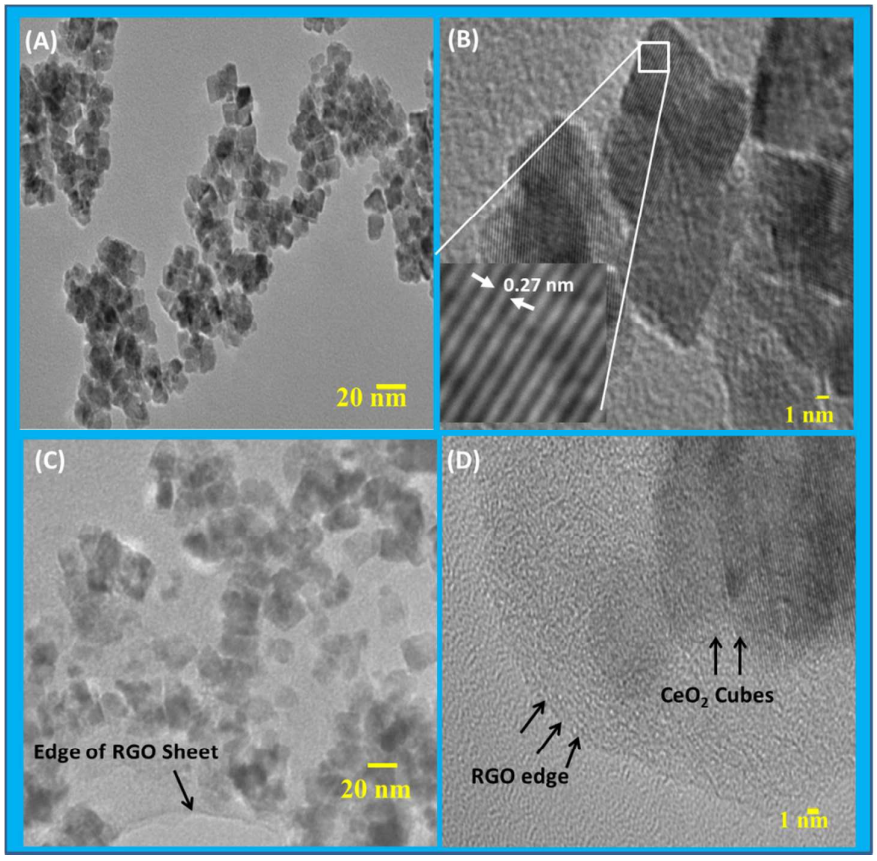

Fig. 4: TEM images (A) and (B) $ncCeO_2$ at 20 nm and 1 nm scale, (C) and (D) $ncCeO_2$-RGO nanocomposite at 20 nm and 1 nm scale.

Journal of Materials Chemistry B Accepted Manuscript

View Article Online
DOI: 10.1039/C8TB00653A

Published on 06 April 2018. Downloaded by Freie Universitaet Berlin on 06/04/2018 16:55:19.

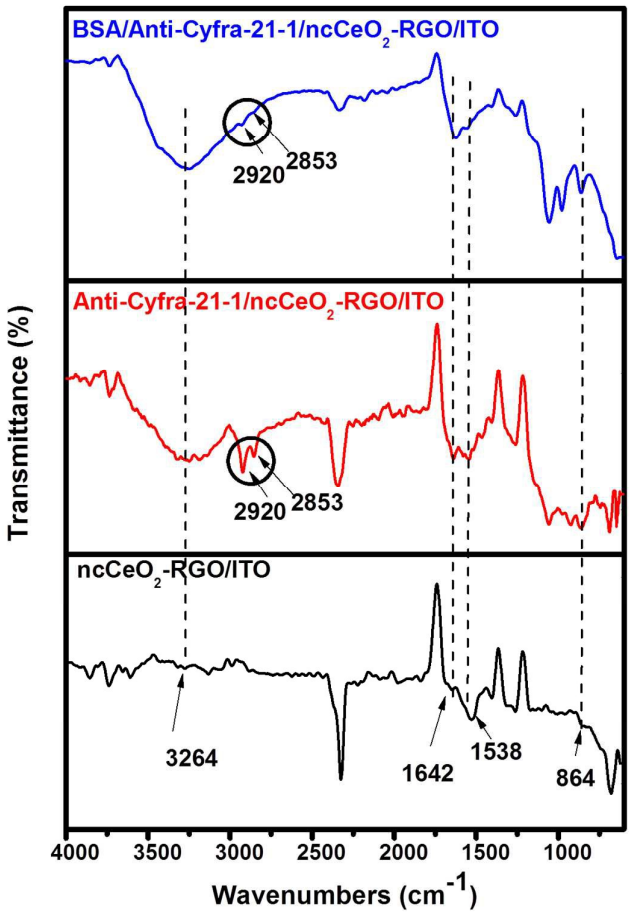

Fig. 5: FTIR graph of $ncCeO_2$-RGO/ITO, Anti-Cyfra-21-1/$ncCeO_2$-RGO/ITO and BSA/Anti-Cyfra-21-1/ $ncCeO_2$-RGO/ITO immunoelectrodes.

Journal of Materials Chemistry B Accepted Manuscript

View Article Online
DOI: 10.1039/C8TB00653A

Published on 06 April 2018. Downloaded by Freie Universitaet Berlin on 06/04/2018 16:55:19.

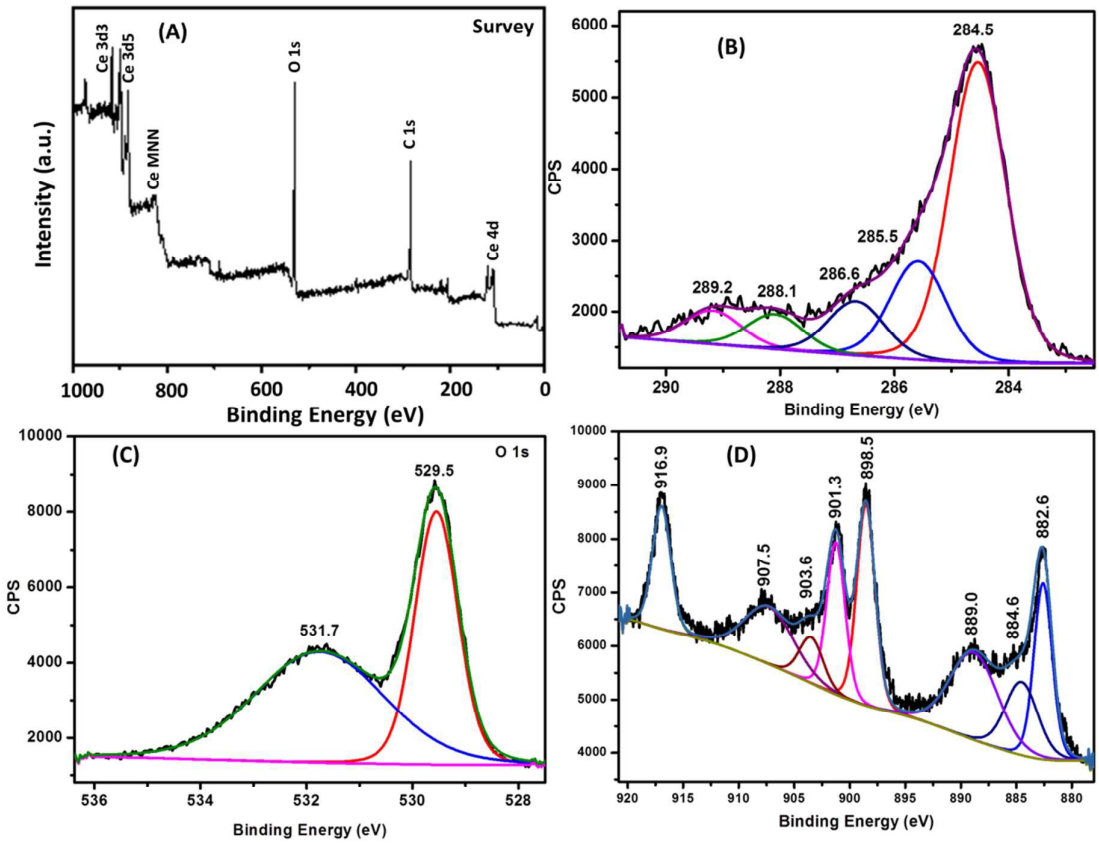

Fig. 6: (A) Complete survey of XPS spectra of ncCeO$_2$-RGO nanocomposite having the peaks of C 1s, O 1s and Ce 3d; Peak fitting of C 1s in (B), O 1s in (C) and Ce 3d in (D).

Journal of Materials Chemistry B Accepted Manuscript

View Article Online
DOI: 10.1039/C8TB00653A

Published on 06 April 2018. Downloaded by Freie Universitaet Berlin on 06/04/2018 16:55:19.

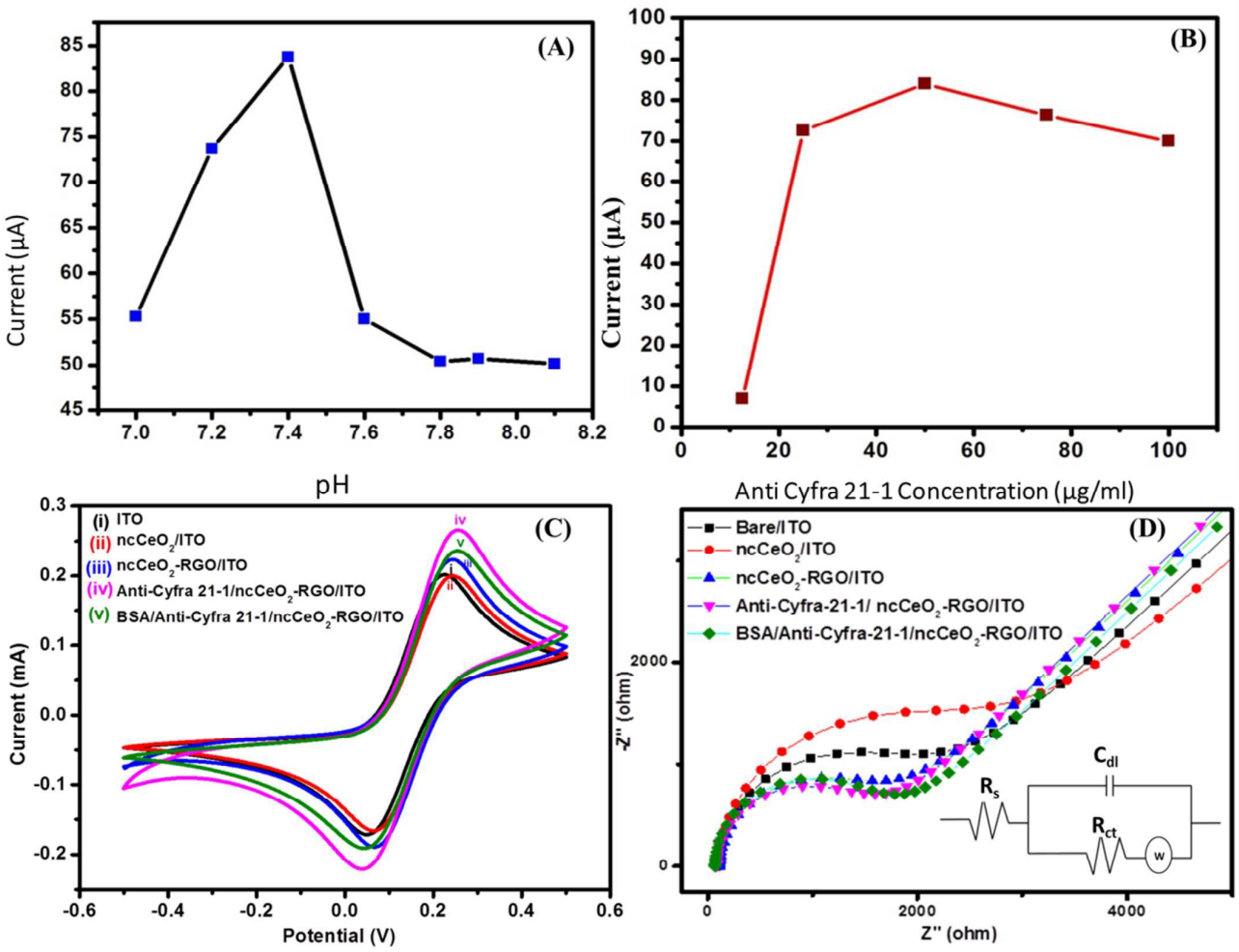

Fig. 7: (A) pH optimization on BSA/Anti-Cyfra-21-1/ncCeO$_2$-RGO/ITO; (B) Different Concentration Antibodies optimization on ncCeO$_2$-RGO/ITO; (C) Comparative CV of Bare-ITO, CeO$_2$/ITO, ncCeO$_2$-RGO/ITO, Anti-Cyfra-21-1/ncCeO$_2$-RGO/ITO and BSA/Anti-Cyfra-21-1/ ncCeO$_2$-RGO/ITO; (D) EIS studies.

Journal of Materials Chemistry B Accepted Manuscript

View Article Online
DOI: 10.1039/C8TB00653A

Published on 06 April 2018. Downloaded by Freie Universitaet Berlin on 06/04/2018 16:55:19.

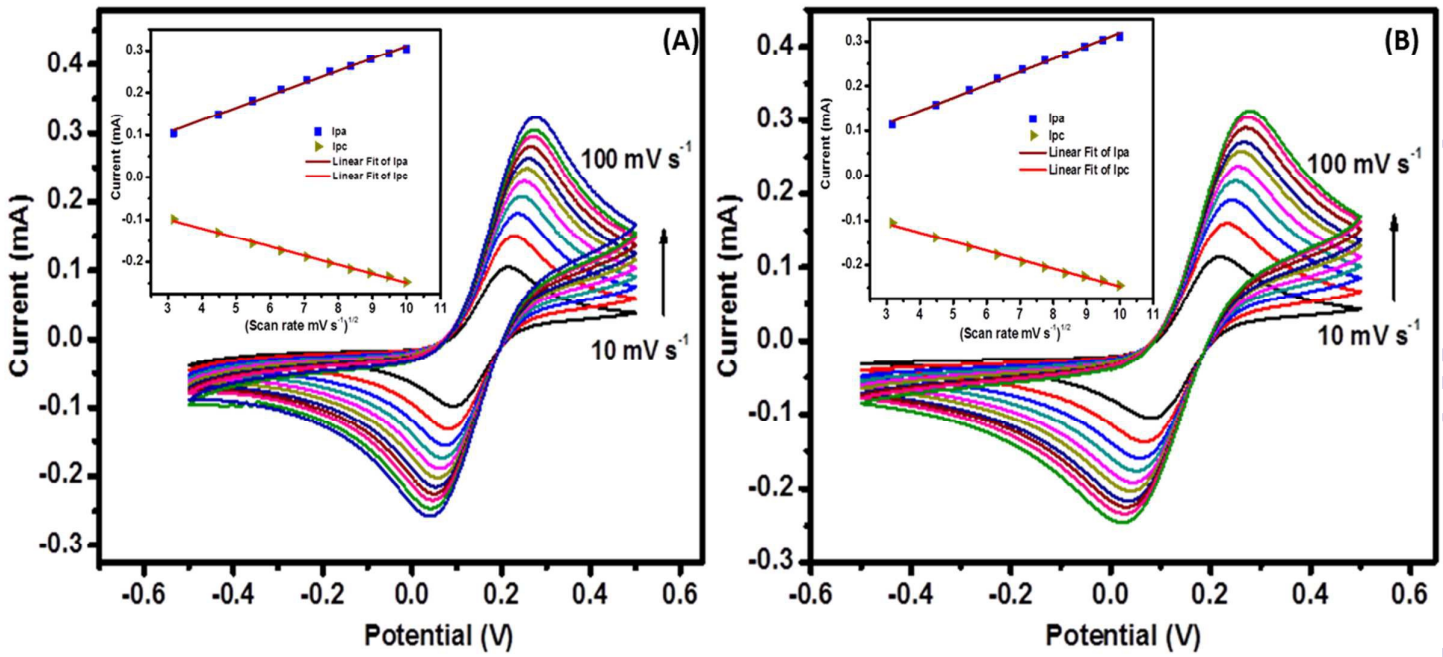

Fig. 8: Scan rate graph; (A) $ncCeO_2$-RGO/ITO and (B) Anti-Cyfra-21-1/$ncCeO_2$-RGO/ITO

Journal of Materials Chemistry B Accepted Manuscript

View Article Online
DOI: 10.1039/C8TB00653A

Published on 06 April 2018. Downloaded by Freie Universitaet Berlin on 06/04/2018 16:55:19.

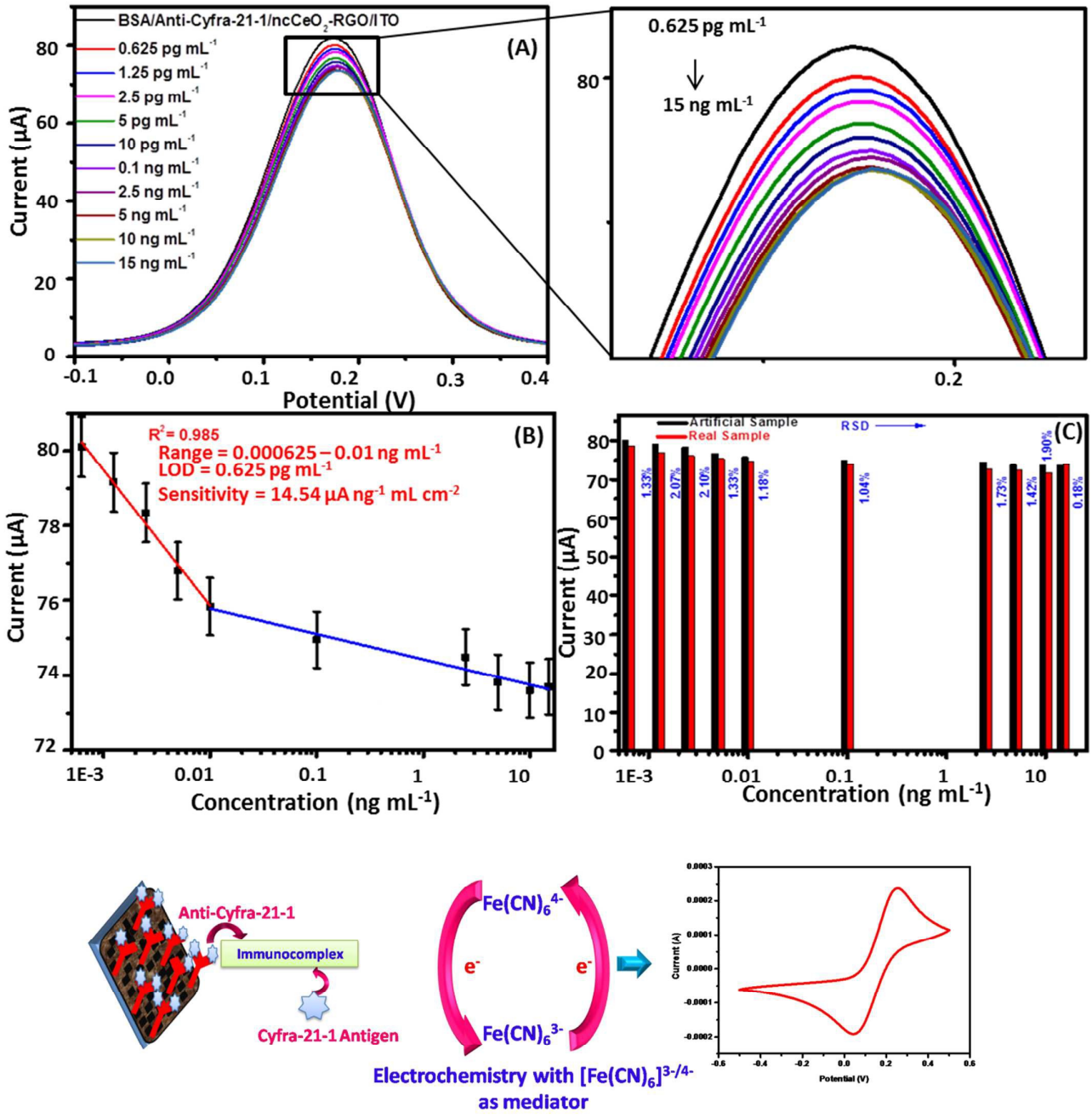

Fig. 9: (A)DPV response studies of the BSA/Anti-Cyfra-21-1/ncCeO$_2$-RGO/ITO toward different concentrations (0.625 pg mL^{-1} to 15 ng mL^{-1}) of Cyfra-21-1 in PBS solution containing $[Fe(CN)_6]^{3-/4-}$ with pH 7.4 (B) Linear curve and (C) Comparison with spiked sample.(D) Tentative Mechanism of electrochemical sensing of Cyfra-21-1 onto BSA/Anti-Cyfra-21-1/ncCeO$_2$-RGO/ITO immunosensor in the presence of $[Fe(CN)_6]^{3-/4-}$.

Journal of Materials Chemistry B Accepted Manuscript

View Article Online
DOI: 10.1039/C8TB00653A

Published on 06 April 2018. Downloaded by Freie Universitaet Berlin on 06/04/2018 16:55:19.

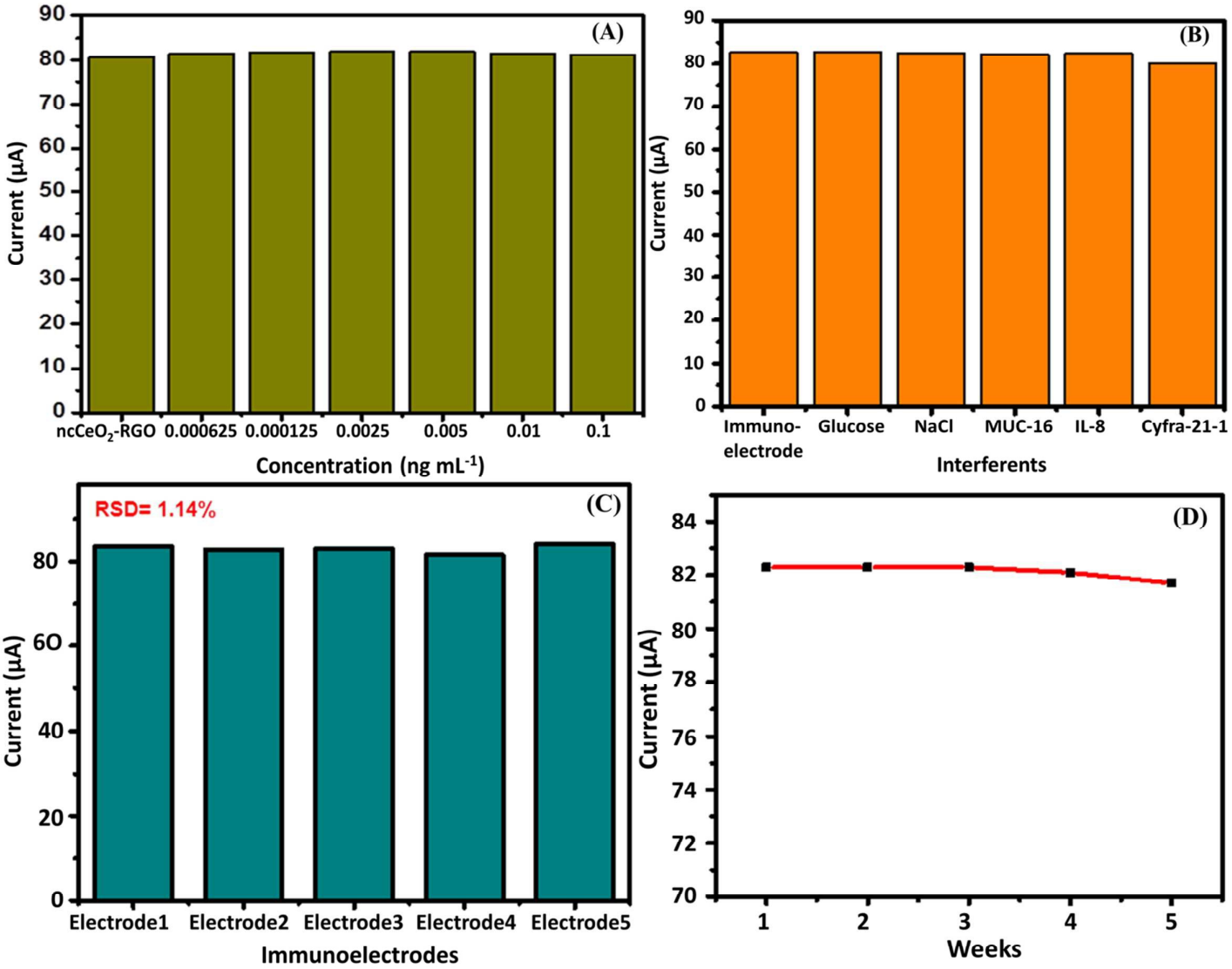

Fig. 10: (A) Control Study: Effect of Cyfra-21-1 concentration on $ncCeO_2$-RGO/ITO electrode (B) Selectivity Curve and (C) Reproducibility Curve and (D) Shelf life of the BSA/Anti-Cyfra-21-1/$ncCeO_2$-RGO/ITO immunoelectrode.

Journal of Materials Chemistry B Accepted Manuscript

View Article Online
DOI: 10.1039/C8TB00653A

Published on 06 April 2018. Downloaded by Freie Universitaet Berlin on 06/04/2018 16:55:19.

Journal of Materials Chemistry B Accepted Manuscript

Table 1: Characteristics of previously reported literature on Cyfra-21-1 oral cancer biomarker detection over the different immunoelectrodes with present work.

Matrix	Detection Range	Technique	Limit of Detection	Sensitivity	Reference
BSA/anti-CYFRA-21-1/APTES/ZrO_2/ITO	2-16 ng mL^{-1}	CV	0.08 ng mL^{-1}	2.2 mA mL ng^{-1}	34
BSA/anti-Cyfra-21-1/APTES/nHfO_2/ITO	2-18 ngmL^{-1}	CV	0.21 ngmL^{-1}	9.28 µA mL ng^{-1} cm^2	32
BSA/anti-CYFRA-21-1/APTES/ZrO_2-RGO/ITO	2-22 ng mL^{-1}	DPV	0.122 ngmL^{-1}	0.756 µA mL ng^{-1}	35
BSA/anti-Cyfra-21-1/L-Cys-$La(OH)_3$/ITO	0.001-10.2 ng mL^{-1}	DPV	0.001 ng mL^{-1}	12.04 µA mL ng^{-1} cm^{-2}	33
BSA/Anti-Cyfra-21-1/ncCeO_2-RGO/ITO	0.625pg mL^{-1}-15 ng mL^{-1}	DPV	0.625 pg mL^{-1}	14.54 µA mL ng^{-1} cm^{-2}	Present Work

Table 2: EIS analytical performance of different electrodes.

Electrodes	R_s (Ω)	R_{ct} (KΩ)	C_{dl} (µF)	K_e (constant)	τ (s)
Bare-ITO	100	1.80	1.57	1.18×10^{-7}	2.82×10^{-3}
ncCeO_2/ITO	115	2.32	1.57	0.91×10^{-7}	3.64×10^{-3}
ncCeO_2-RGO/ITO	116	1.42	1.79	1.49×10^{-7}	2.54×10^{-3}
Anti-Cyfra-21-1/ncCeO_2-RGO/ITO	84.6	1.35	2.26	1.57×10^{-7}	3.05×10^{-3}
BSA/Anti-Cyfra-21-1/ncCeO_2-RGO/ITO	58.4	1.45	2.69	1.46×10^{-7}	3.90×10^{-3}

View Article Online
DOI: 10.1039/C8TB00653A

Published on 06 April 2018. Downloaded by Freie Universitaet Berlin on 06/04/2018 16:55:19.

Table 3: Electrochemical response of immunoelectrode for standard Cyfra-21-1 and spiked sample

Concentration of Cyfra-21-1 (ng mL^{-1})	Highest current for standard Cyfra-21-1 (µA)	Highest current for spiked sample (µA)	Relative standard deviation (RSD %)
0.000625	80.1086	78.6133	1.33
0.00125	79.1626	76.8738	2.07
0.0025	78.3386	76.0498	2.10
0.005	76.7822	75.3479	1.33
0.01	75.8362	74.585	1.18
0.1	74.9512	73.8525	1.04
2.5	74.4934	72.6929	1.73
5	73.822	72.3572	1.42
10	73.6084	71.6553	1.90
15	73.7	73.8831	0.18

Journal of Materials Chemistry B Accepted Manuscript